IOSR Journal of Applied Physics (IOSR-JAP)
e-ISSN: 2278-4861.Volume 18, Issue 3 Ser. 1 (May – June 2026), PP 01-15
www.Iosrjournals.Org

Tailoring spinel Co–Zn ferrite nanocomposites through yttrium substitution: Insights into structure–property relationships

B.M. Bindushree, L.R. Naik
Department of Physics, J.S.S. Banashankari Arts, Commerce and Shanti Kumar Gubbi Science College, Dharwad, 580004, India.
Department of Studies in Physics, Karnatak University, Dharwad 580003, Karnataka, India.

Abstract
Yttrium-doped cobalt zinc ferrites with the composition $Co_{0.6}Zn_{0.4}Y_xFe_{2-x}O_4$ (x = 0, 0.1, 0.2, 0.3) were successfully synthesized via the sol–gel method, and their structural, dielectric, electrical, and microstructural properties were systematically investigated. X-ray diffraction confirmed the formation of a single-phase cubic spinel structure, with crystallite sizes decreasing from 57.961 to 27.507 nm as yttrium content increased, indicating lattice distortion induced by Y^{3+} substitution. A slight reduction in lattice parameter from 8.412 to 8.389 Å was observed, consistent with the substitutional effect. Additional structural parameters such as interplanar spacing, X-ray density, bond lengths, and porosity were also evaluated. FTIR spectra revealed two characteristic absorption bands ~586.253 Cm^{-1} and ~418.477 Cm^{-1} corresponding to tetrahedral and octahedral metal– oxygen vibrations, further supporting successful spinel formation. FESEM analysis showed agglomerated nanoscale particles, while EDAX confirmed the presence of Co, Zn, Fe, Y, and O in the ferrite lattice. Dielectric measurements exhibited normal dispersion behaviour, with high permittivity at low frequencies and stabilization at higher frequencies. AC conductivity increased linearly with frequency, suggesting a small-polaron hopping conduction mechanism followed by the Maxwell–Wagner interfacial polarization mechanism. UV–Visible diffuse reflectance analysis shows the optical band gap ranging from 1.3074 to 1.2291 eV. The hysteresis curves of yttrium doped Co-Zn nano-ferrites demonstrate a minimal coercivity and remanent magnetization, indicating a superparamagnetic behaviour persisting at room temperature. Overall, the findings demonstrate that yttrium doping effectively tailors the structural and electrical characteristics of Co–Zn ferrites, making them promising candidates for high-frequency electronic, magnetic and functional device applications.

Keywords: *Nano ferrites, sol-gel method, elastic properties, optical band gap, saturation magnetisation.*

Date of Submission: 24-04-2026 Date of Acceptance: 04-05-2026

I. Introduction

Ferrites constitute a category of ceramic magnetic materials primarily composed of iron oxide (Fe_2O_3) in combination with other metal oxides such as nickel, zinc, manganese, or cobalt. These materials crystallize in a spinel structure, which is characterized by a cubic close-packed arrangement of oxygen ions, with metal cations occupying interstitial tetrahedral and octahedral sites. Ferrites exhibit ferrimagnetism, wherein the magnetic moments of ions on different sublattices align in opposite directions but with unequal magnitudes, resulting in net magnetization. Owing to their high electrical resistivity and favourable magnetic properties, ferrites are extensively utilized in various technological applications, including transformers, inductors, magnetic recording media, electromagnetic interference (EMI) suppression, and microwave devices. Their tuneable magnetic and electrical characteristics render them indispensable materials in electronics and telecommunications [1].

Cobalt nickel ferrite is a prominent member of the ferrite family, which comprises ceramic magnetic materials primarily constituted of iron oxide combined with metal oxides such as cobalt and nickel. These ferrites crystallize in a spinel structure; wherein metal cations occupy tetrahedral and octahedral sites within a cubic close-packed oxygen ion lattice. The incorporation of cobalt and nickel in ferrites enhances their magnetic properties due to the specific magnetic moments and interactions of these metal ions. The significance of cobalt nickel ferrite lies in its tuneable magnetic and electrical characteristics, rendering it highly valuable for various technological applications. Its ferrimagnetic nature, characterized by unequal and oppositely aligned magnetic moments on different sublattices, results in net magnetization suitable for devices requiring stable and controllable magnetic behaviour. Furthermore, cobalt nickel ferrite exhibits high electrical resistivity, thereby reducing eddy current losses, which is crucial for high-frequency applications. Owing to these properties, cobalt nickel ferrite is extensively utilized in transformers, inductors, electromagnetic interference (EMI) suppression, magnetic recording media, and microwave devices. Its capacity to be tailored for specific magnetic and electrical

performance makes it indispensable in electronics and telecommunications, where efficient signal processing and noise reduction are critical [2,3].

The modification of ferrite crystal lattice structures can be accomplished through the incorporation of various rare-earth ions, which subsequently enhance their magnetic, optical, and electrical properties. Trivalent rare-earth metal cations, such as Eu^{+3}, Dy^{+3}, Yb^{+3}, In^{+3}, Pr^{+3}, Sm^{+3}, Gd^{+3}, Nd^{+3}, Tm^{+3}, Ho^{+3}, Er^{+3}, and La^{+3}, are frequently utilized as dopants in ferrites due to their 4-f electronic configuration and larger ionic sizes [4]. Yttrium ions, in particular, are noteworthy as dopants because of their impact on optical properties and magnetic parameters through their f-electron configurations [5,6]. The introduction of dopants such as rare-earth ions into spinel ferrites is an effective strategy for altering their physical properties. Rare-earth ions, such as Y^{3+}, can influence the structural, dielectric, and magnetic properties, as well as the distribution of cations between tetrahedral (A) and octahedral (B) sites, due to their larger ionic radii and magnetic moments [7-9]. It has been observed that substituting yttrium enhances magnetic softness and improves the grain structure without inducing secondary phases [10]

To the best of our knowledge, systematic investigations of yttrium-substituted Co–Zn ferrites remain limited and fragmented. Previous studies by J. V. Devkar et al. 2023 primarily concentrated on the electrical properties of Y-doped Co–Zn ferrites, highlighting their potential for transducer applications. Similarly, P. C. Patil et al. 2025 examined the elastic and magnetic properties of Ce^{+3} and Y^{+3} co-substituted $Co_{0.85}Zn_{0.15}Fe_{2-2x}O_4$ spinel ferrites. However, these investigations were restricted to selective property evaluations and did not provide a comprehensive understanding of the interplay between structural modifications, synthesis methodology, and multifunctional properties. A significant research gap exists in correlating structural parameters (such as lattice expansion, cation redistribution, crystallite size variation, and micro strain) with elastic, optical, electrical conductivity, and magnetic behaviour in Y-substituted Co–Zn ferrites prepared via controlled synthesis routes. Specifically, the influence of synthesis strategy on phase purity, defect chemistry, Fe^{+2}/Fe^{+3} ratio, hopping conduction mechanisms, and exchange interactions has not been systematically addressed in a single study. Therefore, the present work aims to provide a holistic investigation by establishing clear correlations between: Synthesis route → Structural evolution → Cation distribution → Multifunctional properties. This integrated structure–property relationship analysis constitutes the primary novelty of the study and contributes to the rational design of rare-earth substituted spinel ferrites for advanced multifunctional applications such as microwave devices, inductors, transformers, and magnetic recording media, where enhanced performance and stability are essential. The capacity to control its properties through yttrium doping positions it as a promising material for next-generation electronic and telecommunications components. [11,12].

II. Synthesis

To synthesize Y-substituted Co-Zn ferrites, AR-grade Yttrium nitrate, cobalt nitrate, zinc nitrate, and ferric nitrate were employed using the sol-gel method. The metal nitrates were combined in their stoichiometric proportions and dissolved in double-distilled water to form an aqueous solution. This solution was then stirred magnetically at 90°C for 30 minutes to achieve a uniform mixture of metal nitrates. A 10% PVA solution and a sucrose solution were subsequently added to this uniform metal nitrate solution. After two and a half hours of continuous stirring on a magnetic stirrer at 90°C, the solution turned into a dark, tar-like gel, during which nitrogen dioxides were removed. The dark gel was further heated over a Bunsen burner to produce live charcoal. The material was then allowed to cool to room temperature in the air and was ground using an agate mortar for one hour to obtain a fine powder of Y-substituted Co-Zn ferrites. The samples were annealed at 900°C for five hours to achieve the final product. A schematic representation of the synthesis process is provided in Fig. 1 [13].

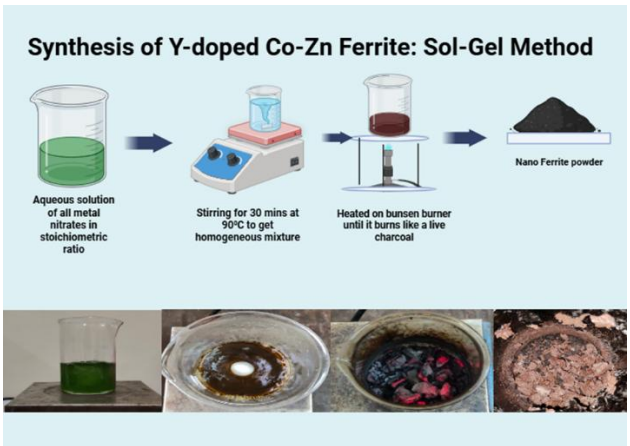

Fig.1: Represents the schematic representation of synthesis of Y-doped Co-Zn ferrite nanoparticles.

III. Results and Discussion

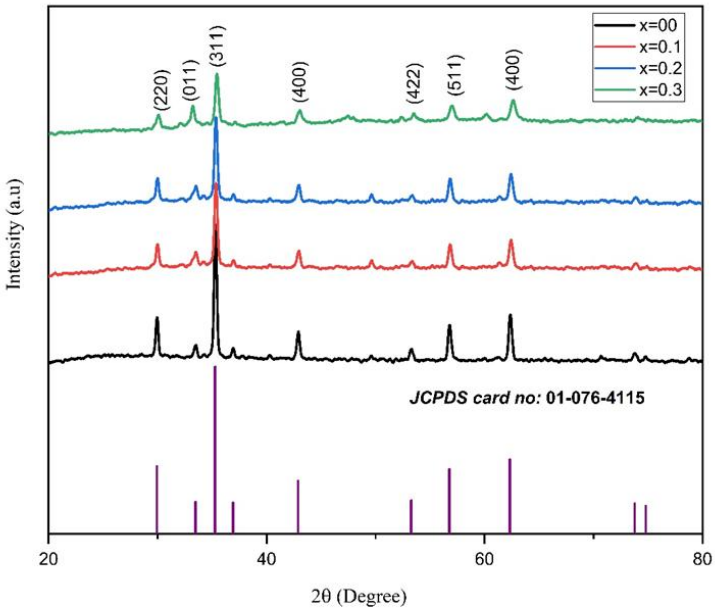

Fig. 2: XRD pattern of Y-doped Co-Zn ferrite samples.

XRD Analysis

The phase composition, crystalline quality, crystallographic orientations and lattice structure of yttrium doped ferrites nanocomposites were studied by the X-ray diffraction analysis. The powder XRD patterns were captured using a Rigaku IV Ultima X-ray diffractometer with Cu-Kα radiation (wavelength λ = 1.5405 Å). **Fig.2** shows the XRD spectra of the as-prepared spinel structured $Co_{0.6}Zn_{0.4}Y_xFe_{2-x}O_4$ ferrites (x = 0.0, 0.1, 0.2. 0.3). All the different planes of synthesized samples in the XRD pattern were indexed with the help of ASTM data and are in good agreement with the standard JCPDS card no 01-076-4115. The prominent peak (311) was observed in all the ferrite samples with various yttrium molar concentrations shows the formation of cubic spinel structure of single-phase ferrite.

The average crystalline size (D) of the nano crystallites is assessed by using the Debye-Scherrer equation. **Fig. 3 and 4** represents the variation of lattice parameter, crystallite size and cell volume as a function of yttrium substitution (x) in Co-Zn ferrite.

$$D = \frac{\lambda \times k}{\beta \cos\theta} \quad (1)$$

$$\beta \cos\theta = \frac{k\lambda}{D} + 4\varepsilon \sin\theta \quad (2)$$

where D is the average crystallite size, k is a shape factor constant of the XRD (0.89), λ is the wavelength (λ= 1.5405 Å), β is the full width half maximum (FWHM) of diffraction peaks, ε is the strain induced inside the samples and θ is Bragg's diffraction angle [14,15].

Further, the lattice parameter, interplanar distance d-spacing (d) and X-ray density (dx) were determined using the following expressions:

$$a = d\ \sqrt{h^2 + l^2 + k^2} \quad (3)$$

$$2d \sin\theta = n\lambda \quad (4)$$

$$dx = 8M/Na^3 \quad (5)$$

where, (h k l) are the Miller indices, 'a' is the lattice parameter and 'd' is interplanar distance, molecular weight of the composition (M) and Avogadro number (N) [16-18].

Also, bond lengths (A-O) & (B–O), interplanar d-spacing (d), site radius (r_A) & (r_B) and porosity were calculated according following equations:

$$(A-0) = (u - \tfrac{1}{4})\ a\sqrt{3} \quad (6)$$

$$(B-0) = (\tfrac{5}{8} - u)\ a \quad (7)$$

$$r_A = (u - \tfrac{1}{4})\ a\sqrt{3} - r \quad (8)$$

$$r_B = (\tfrac{5}{8} - u)\ a - r \quad (9)$$

$$p = 1 - \frac{da}{dx} \times 100\% \quad (10)$$

where oxygen positional parameter (u), radius of oxygen ion (r) are known and d_a is actual density and d_x is X-ray density of the sample [19-23]. All the calculated characteristic values are tabulated in **Table 1(a) and 1(b).**

Table 1 (a): *XRD- characteristic parameters for Y-dopped Co- Zn ferrite.*

Composition X	Crystallite size D (nm) calculation	Crystallite size in D (nm) observed	Interplanar spacing d (Å) calculation	Interplanar spacing d (Å) observed	Lattice Parameter a (Å)	Cell volume $(Å)^3$	Dislocation density (1/ D2) (m-2) (10^{15})
0.0	57.961	59.656	2.191	2.194	8.418	596.671	2.468
0.1	39.629	40.939	2.072	2.073	8.407	594.314	7.480
0.2	51.903	53.617	2.073	2.074	8.412	595.332	4.361
0.3	27.507	28.416	2.067	2.069	8.389	590.568	15.141

Table 1 (b): *XRD- characteristic parameters for Y-dopped Co- Zn ferrite.*

Micro strain ε $(x10^{-3})$	A-O in Å	B-O in Å	R_a in Å	R_b in Å	X- ray density ρ in gms/cm^3	% porosity
0.502	1.846	2.091	0.496	0.741	5.281	57.752
0.931	1.843	2.088	0.493	0.738	5.376	56.351
0.712	1.844	2.089	0.494	0.739	5.441	55.681
1.335	1.839	2.084	0.489	0.734	5.558	58.348

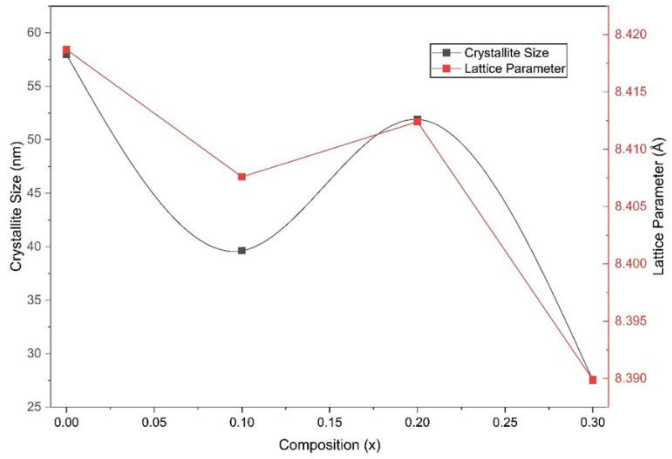

Fig. 3: Shows the variation of crystallite size and lattice parameter with the composition (x).

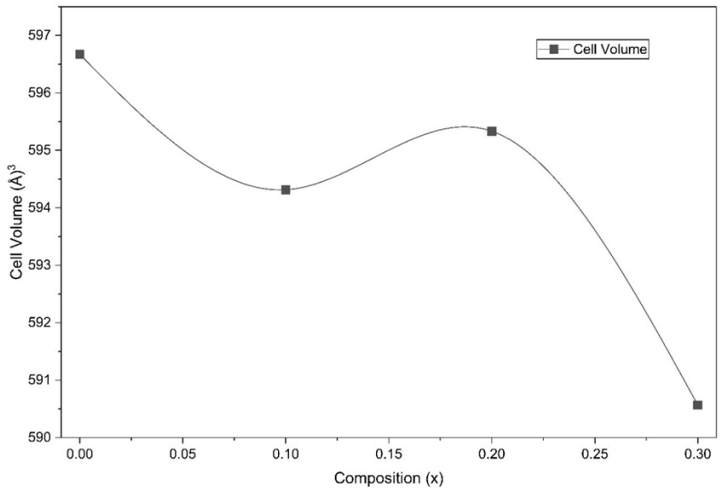

Fig. 4: Shows the variation of cell volume with the composition (x).

From the **Table 1(a and b)** it is observed that the average crystal size (D) of ferrites diminishes as the concentration of yttrium increases. This reduction in particle size may be intentionally hindered due to the presence of Y^{+3}. The primary cause for the reduction in crystalline size is linked to the increase in lattice strain within the sample as more yttrium is added, which involves substituting smaller Co^{+2} ions (0.079 nm) with larger Y^{+3} ions (0.086 nm) in the spinel structure of the $Co_{0.6}Zn_{0.4}Y_xFe_{2-x}O_4$ samples. Based on the calculated data, it was observed that the lattice parameter and interplanar d-spacing values decreased for the Y-doped ferrite composites. This consistent decrease in the lattice parameter is due to the variation in ionic radii of Co^{+2} (0.79 Å), Zn^{+2}(0.74 Å), and Fe^{+3} (0.645 Å), which are smaller compared to Y^{+3} (1.04 Å). The declining trend in the lattice constant value of ferrites follows Vegard's law, with the lattice parameters ranging from 8.41 Å to 8.38 Å [24].

Further, the values of X-ray density were found to increase with increase in Y^{+3}concentration and also it was found that the maximum porosity was obtained for the composition x = 0.3 is 58.34%. Hence can be used in various applications requiring enhanced magnetic properties, such as flux concentrators and advanced electronic components like low-frequency filters and resonant inductors [25].

FTIR Analysis

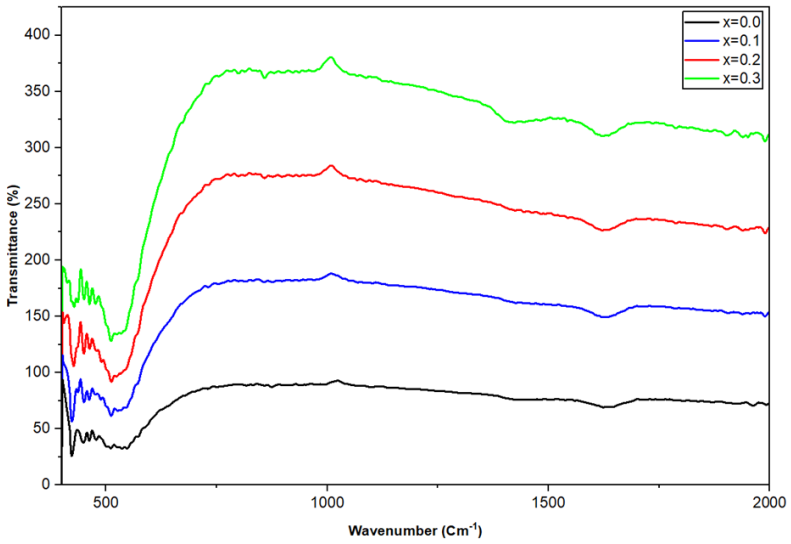

Fig. 5: Shows the FTIR spectra of Y-dopped Co- Zn ferrite.

FT-IR Spectrometer Nicolet 5700 was employed to examine the chemical composition and functional group present in the sample. **Fig. 5** shows the FTIR spectra of the synthesized ferrites nanocomposites with different concentrations of yttrium within the range 2000−400 cm^{-1} wavenumber. The metal ions in ferrites occupy two different interstitial sites namely the tetrahedral site (A-site) while the other is at the octahedral site (B-site) based on the configuration of the nearest neighbouring oxygen in the crystal structure, two prominent absorption bands were observed, one a strong adsorption band in the high frequency region ν_1 around 600 cm^{-1} and is associated with the intrinsic stretching vibrations of the metal-oxygen band in the tetrahedral (A) site where as the weak band observed in the lower frequency ν_2 in the range 400 cm^{-1} to 500 cm^{-1} attributed to metal–oxygen stretching in the octahedral (B) site. Further, no of extra characteristics peaks is observed FTIR spectra of Co–Zn–Y nano ferrites sample. This could be suggestive that the synthesised composite is divide of any impurities and structural defects.

The FTIR analysis of the given ferrite samples also shows distribution of cation in the crystal structure in which Zn^{+2} ion occupies the tetrahedral site (A-site) and the octahedral site (B-site) was occupied by Co^{+2} ions whereas Fe^{3+} ions occupy both octahedral as well as the tetrahedral site. The shift in the metal–oxygen band position towards lower wavelength is may be due to the substitution of smaller Zn^{+2} ion in the crystal structure which in turn results in the displacement of Fe^{3+} ions and decreases the amount of Co^{+2} in the octahedral site (B-site).

Waldron method was employed to calculate the force constants of tetrahedral site (k_t) and octahedral site (k_o), according to which interatomic bonding strength k_t and k_o are given as follows:

$$k_t = 7.62 \times M_1 \times \nu_1^2 \times 10^{-7}\ N\ m^{-1} \quad (11)$$

$$k_o = 10.62 \times M_2/\ 2 \times \nu_2^2 \times 10^{-7}\ N\ m^{-1} \quad (12)$$

Where M_1 and M_2 are the molecular weights of cations in A- and B-sites respectively and ν is frequency. The calculated Inter-atomic force constant k_t and k_o are listed in Table 2. from the table it is noted that the tetrahedral force constant 'k_t' decreases whereas octahedral force constant 'k_o' decreases with increase in yttrium

doping this is due to the disruption of the tetrahedral and octahedral site geometries, as the larger Y^{3+} ion modifies the local coordination environment and inter-ionic distances, thereby reducing the bond stiffness in these sites [26-28]. Further the bulk modulus B is calculated by using the relation:

$$B = C_{11} \quad (13)$$

(where C_{11} is stiffness constant)

$$C_{11} = k_{av}/a \quad (14)$$

Where k_{av} is the average force constant.

$$k_{av} = (k_t + k_o)/2 \quad (15)$$

The longitudinal elastic wave velocity (v_l) is given by the formula:

$$V_l = \sqrt{(C_{11}/\rho)} \quad (16)$$

where ρ is density of x rays [29-32]. The relation for transverse elastic wave velocity (Vt):

$$V_t = V_l \sqrt{3} \quad (17)$$

That for rigidity modulus:

$$G = \rho V t^2 \quad (18)$$

and that for Poisson ratio:

$$\sigma = \frac{(3B-2G)}{(6B+2G)} \quad (19)$$

Young modulus:

$$E = (1 + \sigma)2G \quad (20)$$

Mean elastic wave velocity:

$$V_m = \sqrt[3]{\left(\frac{3Vt^2\, Vl^2}{Vt^2+Vl^2}\right)} \quad (21)$$

Debye temperature given by Anderson's formula:

$$\theta_D = \frac{h}{k_B} \sqrt[3]{\frac{(3N_A)}{(4\prod V_A)}}\ Vm \quad (22)$$

V_A is the mean atomic volume.

Table 2: FT-IR data for Yttrium doped Co-Zn ferrite.

Parameter	X=0.0	X=0.1	X=0.2	X=0.3
v_1(cm-1)	586.2539	576.6116	580.4685	578.54
v_2(cm-1)	418.4773	418.4773	418.4773	418.477
K_t (N/m)	2521.135	2438.885	2471.621	2455.225
K_o (N/m)	1284.601	1284.601	1284.601	1284.599
K_{av} (N/m)	1902.868	1861.743	1878.111	1869.912
V_l (m/s)	6547.041	6415.431	6414.143	6328.697
V_t (m/s)	3779.936	3703.951	3703.207	3653.875
V_m (m/s)	4196.446	4112.087	4111.262	4056.494
B (GPa)	225.874	221.537	222.983	223.008
G (GPa)	75.291	73.846	74.328	74.336
E (GPa)	203.286	199.383	200.684	200.708
σ	0.351	0.351	0.351	0.351
Θ_D (K)	567.317	557.284	555.921	550.983
Θ'_D (K)	723.276	716.335	719.111	717.723

Furthermore, using FTIR spectrographs the elastic properties of ferrite materials such as bulk modulus (B), modulus of rigidity (G), Young's modulus (E), Poisson's ratio (σ), longitudinal elastic wave velocity (V_l), transverse elastic wave velocity (V_t), mean elastic wave velocity (V_m), and Debye temperature (θ) are estimated [33-38] and the same is listed in **Table 2**. The table shows that as the yttrium doping concentration in the ferrite sample increases, the modulus of rigidity (G), bulk modulus (B), and Young's modulus (E) were observed to decrease as the yttrium doping concentration in the ferrite sample increases, the modulus of rigidity (G), bulk modulus (B), and Young's modulus (E) were observed to decrease this is due to the disruption of the crystal lattice and the weakening of inter-ionic forces, attributed to the larger ionic radius of the Y^{3+} dopant compared to the substituted cations [26].

The Poisson's ratio values for all ferrites are 0.25, but in the current investigation the calculated Poisson's ratio was 0.351 and was constant for all ferrites samples, revealing the isotropic elasticity theory [39].

FESEM and EDAX

The study of the microstructure, surface morphology, and elemental composition of synthesized ferrite nanoparticles is conducted using EDAX spectroscopy and an electron microscope (Zeiss EVO LS 15). **Fig. 6** illustrates the FE-SEM images of $Co_{0.6}Zn_{0.4}Y_xFe_{2-x}O_4$ samples for x values of 0, 0.1, 0.2, and 0.3. [40,41]. The SEM images show agglomeration of the samples, it may be due to the diffusion mechanisms like grain boundary

and volume diffusion during the process of sintering [13,46].

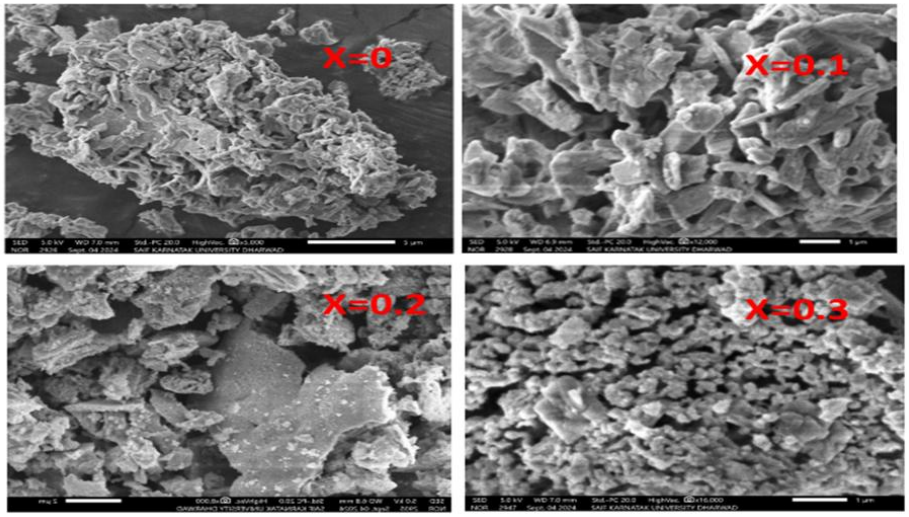

Fig. 6: Shows the SEM images of Y-dopped Co- Zn ferrite samples.

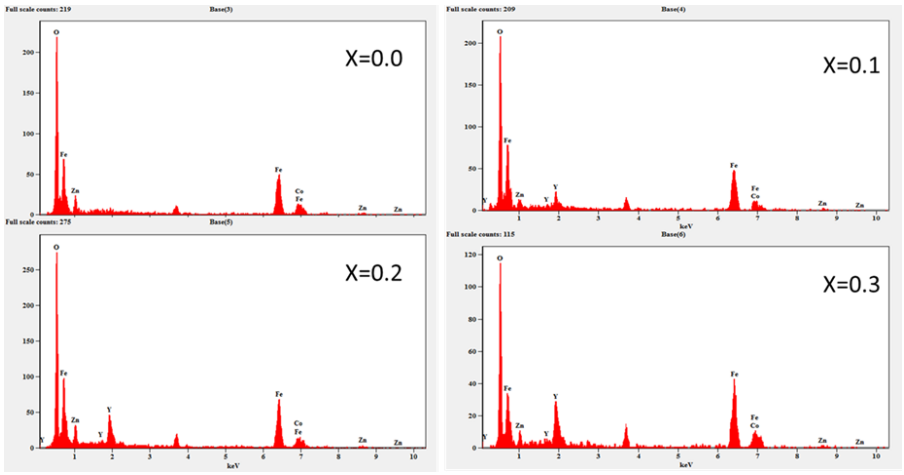

Fig. 7: Shows the EDAX images of Y-dopped Co- Zn ferrite samples.

Additionally, energy dispersive X-ray spectroscopy (EDAX) was employed to analyse the elemental composition of the Y^{+3} doped Co-Zn ferrite samples post-final sintering, as depicted in **Fig. 7**. The comprehensive EDAX profile obtained confirms the presence of cobalt (Co), Zinc (Zn), iron (Fe), yttrium (Y), and oxygen (O) within the nano ferrite lattices. The findings also verify the presence of the necessary elements in the prepared composition, with no detectable impurities, indicating the samples' purity. The atomic and weight percentages of Zn^{+2}, Co^{+2}, Y^{+3}, Fe^{+3}, and O^{-2} ions in the synthesized composites align with the stoichiometric ratio, as illustrated in **Fig. 7**. Typically, ferrites exhibit a 3:4 metal cation to anion ratio [42]. It is noted that the average cation to anion ratio is 2:4.9. The table presents the atomic percentages of metal anions and cations obtained. For Y-substituted Co-Zn ferrites, these values correspond closely with the standard ratio [43-45]. Table 3 shows the cations-anions atomic percentage of the yttrium doped Co-Zn ferrites.

Table 3: Cations-anions atomic (%) and cations to anions ratio of Y-dopped Co- Zn ferrite samples.

Composition	Cations (%)	Anions (%)	The ratio of cations: anions
X=0.0	29.55	70.44	2.068:4.931
X=0.1	29.18	70.82	2.042:4.956
X=0.2	26.91	73.09	1.882:5.115
X=0.3	33.06	66.96	2.313:4.511

Optical Properties

In order to get the better understanding of effect of Y doping on the optical performances and bandgap of the as-prepared a series of $Co_{0.6}Zn_{0.4}Y_xFe_{(2-x)}O_4$ (x = 0.0, 0.1, 0.2 & 0.3) nano ferrites the UV–Vis DRS measurements were conducted using a UV-Visible spectrometer (DRS) model Agilent Cary Series. Fig 8 shows

the absorption spectra of the composites and optical band gap (Eg) values of all the prepared ferrites was calculated using Tauc's relation.

$$\alpha h\nu = A\,(h\nu - E_g)^{n} \tag{23}$$

Where, α = constant, hυ = energy of incident photon, A = Absorption coefficient, h = Planck's constant [47]. **Fig. 9** displays Tauc plot of as-obtained samples and the energy band gaps are found to be 1.3074, 1.3232, 1.3067 and 1.2291 eV for ferrite samples, respectively. The value of the direct band gap is affected by many factors such as crystallite size, structural parameters, interface effect and absence of purity etc [48]. Recent investigations into rare-earth substituted spinel ferrites have demonstrated similar non-linear band gap behaviour, corroborating that optical transitions are predominantly influenced by structural modifications and the redistribution of electronic density-of-states [49]. Consequently, the observed reduction in band gap with increased Y^{3+} content in the current Co–Zn ferrite system aligns with the dopant-induced defect chemistry and alterations in electronic structure. The obtained energy band gap values reveals that all the synthesized Y-doped Co-Zn ferrites are sensitive to UV energy, which can be suitable as a photocatalyst under UV irradiation.

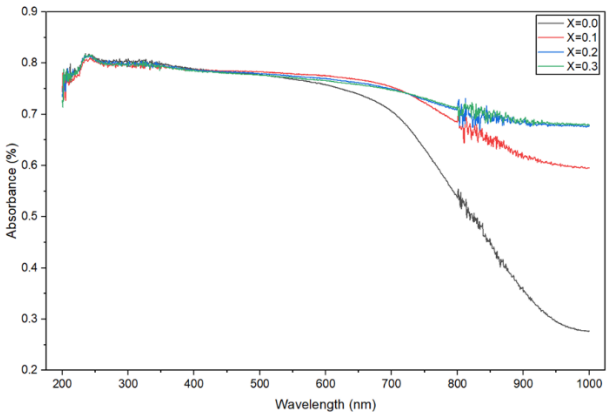

Fig. 8: Shows the absorption spectra of Y-dopped Co- Zn ferrite.

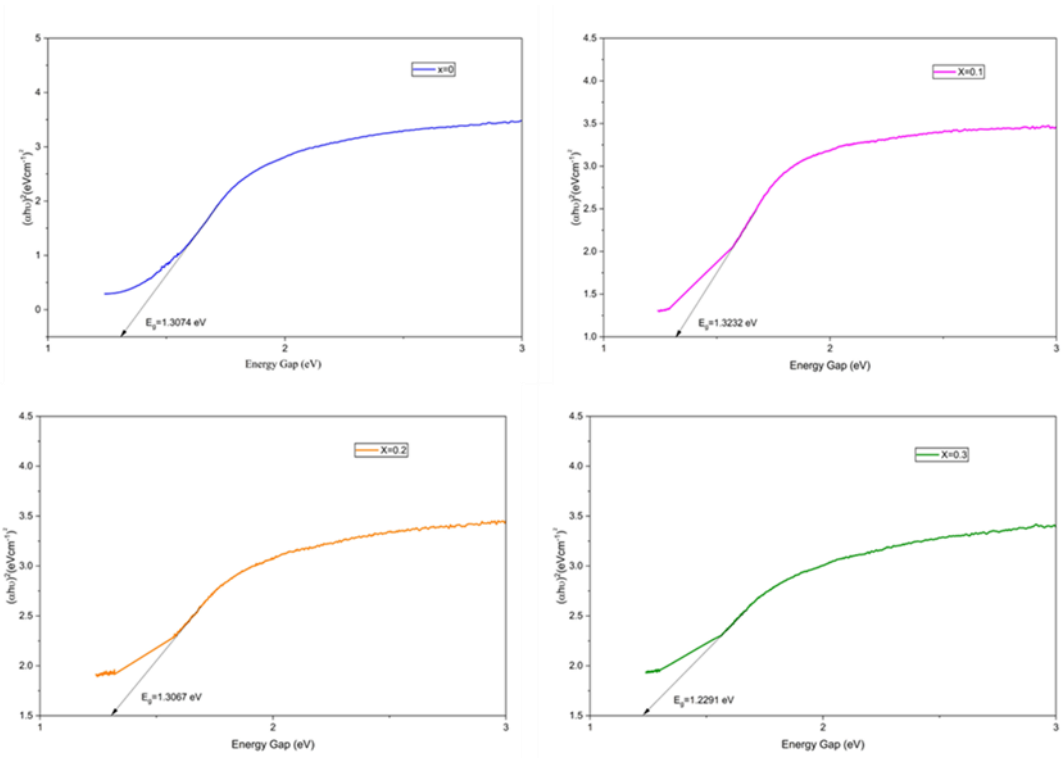

Fig. 9: Shows the Tauc's plot for Y-dopped Co- Zn ferrite

Dielectric and AC Conductivity studies

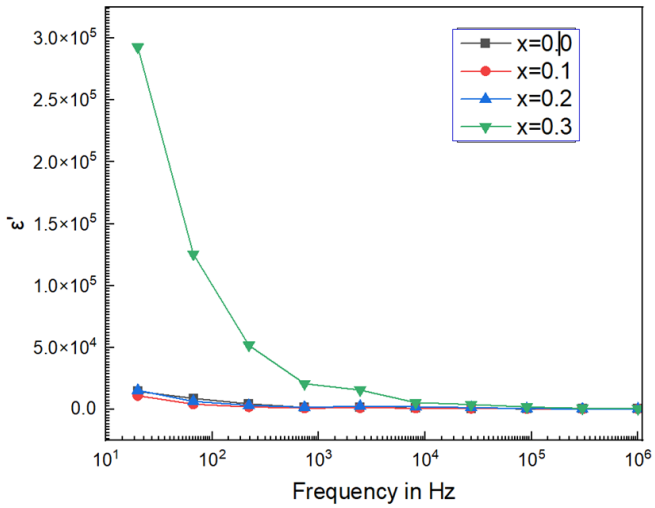

Fig .10: Represents the variation of dielectric constant with respect to frequency for Y-dopped Co- Zn ferrite.

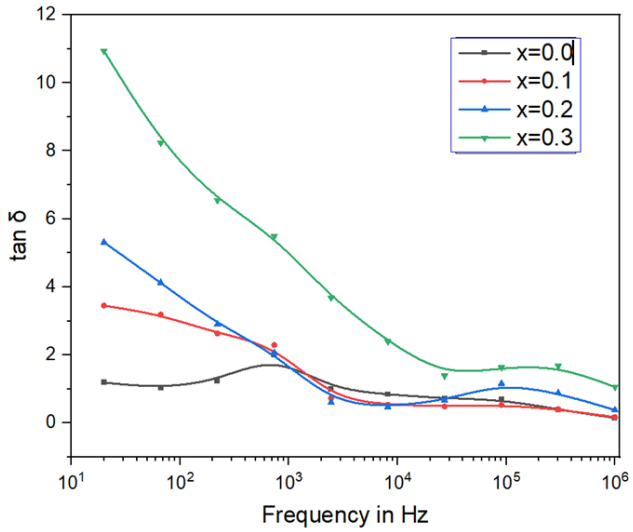

Fig .11: Represents the variation of loss tangent with respect to frequency for Y-dopped Co- Zn ferrite.

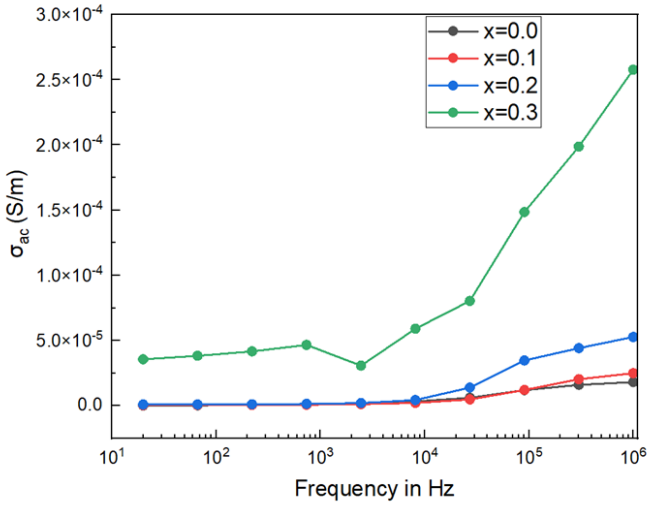

Fig .12: Represents the variation of ac conductivity with respect to frequency for Y-dopped Co- Zn ferrite.

The present study also includes the investigation of electrical behaviour of $Co_{0.6}Zn_{0.4}Y_xFe_{(2-x)}O_4$ (x = 0.0, 0.1, 0.2 & 0.3) nano ferrites using PsimetriQ NAL PSM1700. **Fig. 10**. Displays the variations of dielectric constant of all Y-doped Co-Zn ferrite samples a with respect to frequency which is mainly due to the heterogeneous structure of the ferrites. As shown in the figure, the real dielectric constant initially decreases at lower frequencies and then becomes constant as the frequency increases. A rapid reduction in the dielectric constant in low frequency region (10^1 Hz-10^2 Hz) shows the usual behaviour of dielectric dispersion. Also, at high frequency region the dielectric constant gradually decreases and attains saturation of the ferrite materials (10^3 Hz-10^6 Hz). This variation the dielectric constant can be described on the basis of Maxwell–Wagner model [50] of interfacial polarization which is in good agreement with Koops phenomenological [51] theory. For the purpose of better amplification / visualization of the impact of Yttrium doping level on the dielectric behaviours, the variation in dielectric constant (ε') with frequency was studied for all the samples. And from the result one can realize that, the sample with x = 0.3 shows more dielectric dispersion and it is due to the availability of large number of ferrous ions on A-site of the system. The dielectric constant for all the sample was deduced using the following formula:

$$\varepsilon' = \frac{Cp \times t}{\varepsilon_o A} \tag{24}$$

Where ε' dielectric constant, t is thickness of the pellets, ε_o is permittivity of free space, C_p is parallel capacitance, and A is area of the sample [52].

In general, the greater value of dielectric constant at lower frequency the ferrites are mainly due to the hopping of electrons between Fe^{2+}---→Fe^{3+} ions. The presence of Fe^{3+} and Fe^{2+} ions shows ferrite materials dipolar nature. The interfacial dislocation of Fe^{2+} ions pileups, oxygen vacancies, grain boundaries, defects, etc. Space charge polarization, which leads to an increase in the dielectric constant, is caused by the transfer of electrons between ferrous and ferric ions at the grain boundary area.

Further, the variation of the dielectric loss tangent (tan δ) with frequency for the ferrite samples was studied and the same is shown in **Fig. 11**. A similar trend as that of the dielectric constant was detected for dielectric loss tangent for all the ferrite sample. It was noted form the graph that the dielectric loss tangent shows a decreasing trend with increase in frequency for all the ferrite samples and this is explained by Iwauchi [53]. Also, there is a strong correlation between dielectric behaviour and the conduction mechanism in ferrite. The dielectric loss tangent of all the sample was estimated using the following expression [54]:

$$\tan\delta = \frac{d}{Z\varepsilon_o \omega A} \tag{25}$$

As per the earlier reports the doping of rare earth ions in crystal lattice alters the optical and electrical properties. Thus, the variation of frequency dependent ac conductivity was studied for all the ferrite sample and is displayed in the **Fig.12**. Form the plot, it can be clearly realized that there is a linear increase in AC conductivity of all the ferrite samples with increased frequency which is expected conventional behaviour of any electrical oxide materials [55-56]. The dielectric constant and dielectric loss factor values can be used to determine the AC conductivity and the relation is given below:

$$\sigma_{ac} = \varepsilon\, \varepsilon_o\, \omega \tan\delta \tag{26}$$

Where, ε- dielectric constant, ε_o- permittivity of free space, ω- frequency of the applied field.

The behaviour of the thermally activated conduction mechanism and the kind of polaron hopping that drives electron conduction in the ferrite system is explained by the frequency-dependent variation of AC conductivity. According to Austin Mott and Appel [57], the small polaron hopping type of conduction mechanism in ferrites was responsible for the increase in AC conductivity with frequency, while the large polaron hopping type of conduction mechanism was responsible for the decrease in conductivity with frequency [58]. At the octahedral location, the exchange of electrons between the Fe^{2+} and Fe^{3+}cations drives the conduction mechanism process in yttrium-doped cobalt ferrites.

Magnetic property

The Magnetization measurements of all the synthesized $Co_{0.6}Zn_{0.4}Y_xFe_{(2-x)}O_4$ ($0 \le x \le 0.3$) nano ferrites were studied using Vibrating Sample Magnetometer (Micro-Sense Model FCM-10 Magnetic Field Control Module). The obtained room temperature magnetic hysteresis (M–H loop or M–H hysteretic curve) of the synthesized samples is depicted in **Fig. 13.** The field dependence of magnetization graph shows the ferrimagnetic nature of all the samples.

Table 4: The magnetic parameters of Y-dopped Co- Zn ferrite samples.

Composition x	H_c (O_e)	M_s (emu/g)	M_r (emu/g)	K_a (erg/cm3)	η_B (Bohr magneton)	R
0.0	208.8141	45.7281	6.6499	9743.5254	1.9421	0.1454
0.1	413.7961	31.3199	7.8857	13224.5401	1.3487	0.2518
0.2	498.1781	22.4406	2.6681	11407.5645	0.9796	0.1189
0.3	267.6361	18.8812	7.1767	5156.4171	0.8354	0.3801

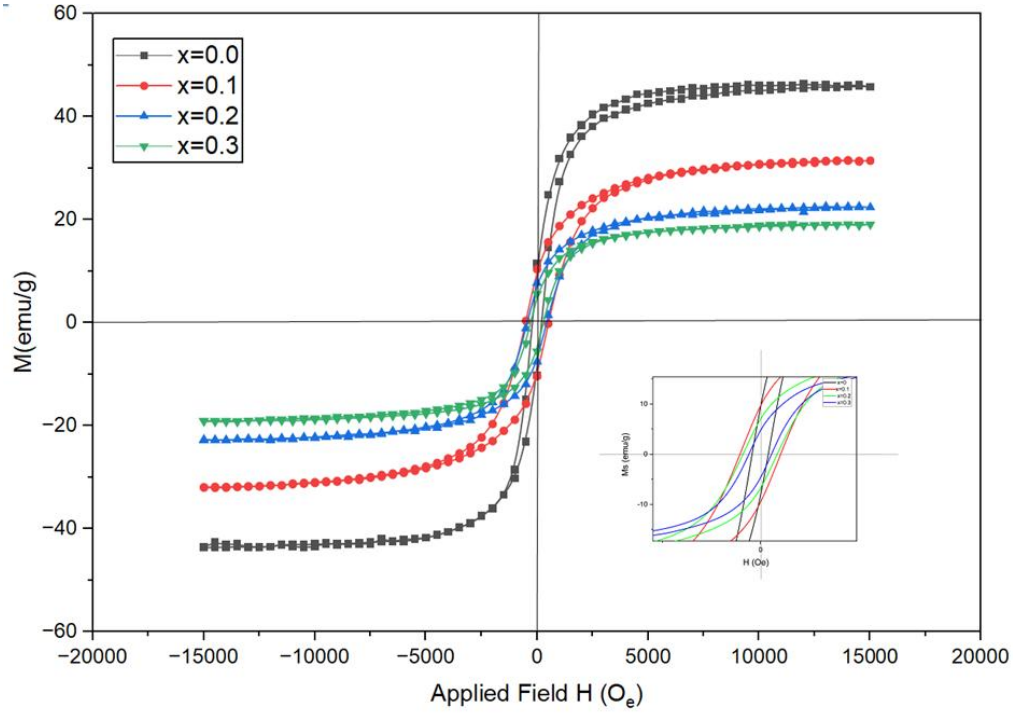

Fig. 13: Represents the hysteresis curve of Y-dopped Co- Zn ferrite samples.

The different parameters such as saturation magnetization (M_s), magnetic moment (η_b), and remnant magnetization (M_r), coercivity (H_c), anisotropy constant (K_α) and remanence ratio (R) of all the synthesized samples was acquired from hysteresis loops at room temperature and is listed in **Table 4. Fig. 14** Shows the variation of saturation magnetisation and remanent magnetisation with change in composition (x) and **Fig. 15** Shows the variation of coercivity and remanence ratio with change in composition (x).

In comparison to the original ferrite (x = 0), the saturation magnetization (M_s) of composites with Y^{+3} substitution is reduced due to the non-magnetic nature of Y^{+3} ions replacing the magnetic Fe^{3+} ions. The table 4 clearly shows that the decrease in M_s, as the saturation magnetization (M_s) gradually declines from 46.19 to 18.27 emu/g with increasing Y^{+3} (x = 0.0, 0.1, 0.2 & 0.3). The variation in saturation magnetization (M_s) with Y^{+3} content is likely due to the surface spin effect and the exchange interactions of cations on A-sites and B-sites. The overall magnetic moment of the material is primarily influenced by the magnetic interactions between A-A, B-B, and A-B sites, as well as the interaction of magnetic ions with an externally applied field. In Co-Zn ferrites, Fe^{+3} ions are present at both A-site and B-site, but Y^{+3} tends to occupy only the B-site. The introduction of trivalent Y^{+3} metal ions in ferrites replaces some Fe^{+3} from the B-site, leading to a reduction in magnetization at the B sub-lattice. This follows Neel's two-sublattice model, where the difference between B site and A site magnetization determines the resultant magnetization. The magnetic moment can be calculated using the equation $M = M_B - M_A$, where M_B and M_A represent the magnetic moments of the B sub-lattice and A sub-lattice, respectively [46]. The remanent magnetization also reduced from 6.6499 for x = 0 to 2.6681 for x = 0.2 emu/g with Y+3 ion substitution and increased for x = 0.1 and x = 0.3 this can be explained by the redistribution of cations within the tetrahedral and octahedral sites of the spinel structure, influencing the super-exchange interactions [59]. The external factors such as microstructure of the grains, porosity, homogeneity, morphology, density, and distribution of cations at lattice sites, considerably affect magnetic influences the magnetic parameter [60].

Also, the remanence ratio (R) increased with Y^{+3} ion substitution and the values were found to be below 0.5 and this small value (M_r/M_s) shows the existence of multidomain (MD) particles in all the ferrite samples. Furthermore, on enhancing concentration yttrium in the ferrite system the coercivity of the samples increased from 208.814 to 498.178 Oe for x = 0.3 which in turn fundamentally depends on the magneto crystalline anisotropy and the particle size [61]. The hysteresis curves of yttrium doped Co-Zn nano-ferrites demonstrate a minimal coercivity and remanent magnetization, indicating a superparamagnetic behaviour persisting at room temperature.

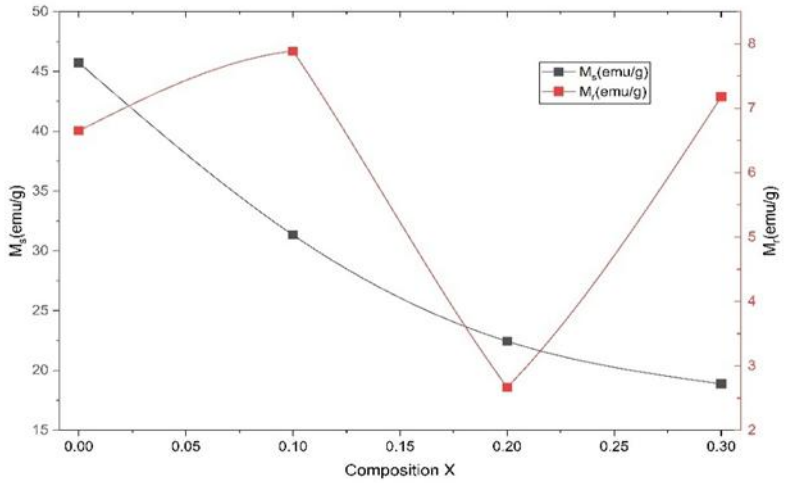

Fig. 14: Shows the variation of saturation magnetisation and remanent magnetisation with change in composition (x)

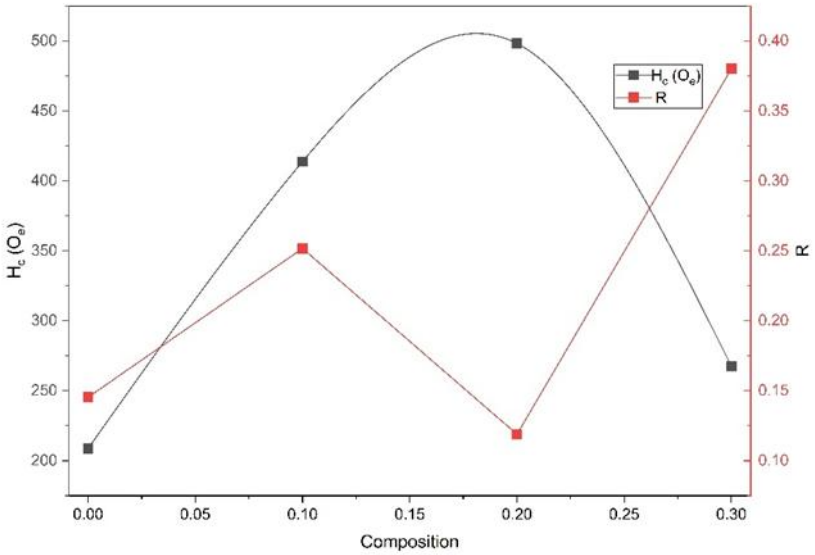

Fig. 15: Shows the variation of coercivity and remanence ratio with change in composition (x)

IV. Conclusion

Yttrium doped cobalt zinc ferrite, $Co_{0.6}Zn_{0.4}Y_xFe_{2-x}O_4$ (x = 0, 0.1, 0.2, 0.3), was synthesized via the Sol-gel method. A range of techniques was employed to characterize the resulting nanocomposites, focusing on their structural, optical, electrical, dielectric and magnetic properties. The Debye-Scherer formula was utilized to determine the average crystallite size, which ranged from 57.961 to 27.507 nm, with lattice constants between 8.412 and 8.389 Å. The results indicated a decrease in the average crystal size (D) of the ferrites with increasing yttrium concentration. Additional parameters, including interplanar distance, X-ray density, bond length, and porosity, were also calculated. Two absorption bands corresponding to tetrahedral and octahedral sites were identified, corroborating the formation of a single-phase cubic structure, and elastic parameters were obtained from FTIR data. FESEM combined with EDAX spectroscopy was employed to analyse the microstructure, surface morphology and elemental composition of the synthesized ferrite nanoparticles. FESEM images revealed agglomeration of the nano ferrites, while the complete EDAX profile confirmed the presence of Co, Zn, Fe, Y, and O in the ferrite lattices. The variation of the dielectric constant with frequency exhibited typical dielectric dispersion at low frequencies and remained nearly constant at high frequencies. The linear increase in ac conductivity with frequency suggested a small polarons hopping conduction mechanism followed by the Maxwell–Wagner interfacial polarization mechanism. UV–Visible diffuse reflectance analysis shows the optical band gap ranging from 1.3074 to 1.2291 eV. The hysteresis curves of yttrium doped Co-Zn nano-ferrites

demonstrate a minimal coercivity and remanent magnetization, indicating a superparamagnetic behaviour persisting at room temperature. Overall, the findings demonstrate that yttrium doping effectively tailors the structural and electrical characteristics of Co–Zn ferrites, making them promising candidates for high-frequency electronic, magnetic, and functional device applications.

Funding
This research did not receive any specific grant from any funding agencies.

Acknowledgement
The authors thank University scientific instrumentation centre (USIC) and SAIF, Karnatak University, Dharwad, for providing instrumentation facility.

Reference

[1]. Tolani, S. C., Golhar, A. R., & Rewatkar, K. G. (2019). A Review of Morphological, Structural Behaviour and Technological Applications 0f Ferrites. 2104(1). Https://Doi.Org/10.1063/1.5100459.
[2]. Kumar, V., Srivastava, R., Kumar, S., Sarkar, K., & Kumar, R. (2024). A Review on Developments in Spinel Ferrite Nanomaterials: Synthesis, Characterization, And Diverse Applications. International Research Journal on Advanced Engineering Hub (IRJAEH), 2(06), 1659–1664. Https://Doi.Org/10.47392/Irjaeh.2024.0228.
[3]. Hublikar, L. V., Patil, V. B., & Ganachari, S. V. (2023). Zn And Co Ferrite Nanoparticles: Towards the Applications of sensing and Adsorption Studies. Environmental Science and Pollution Research, 30(25), 66994–67007. Https://Doi.Org/10.1007/S11356-023-27201-Z .
[4]. I.G. Jhala, Apexa Maru, Laxmi Hathiya, Harshal B. Desai, N.A. Shah, P.S. Solanki, Ashish R. Tanna, H.H. Joshi, "Structural, Magnetic and Electrical Properties of Gadolinium Doped Cobalt Ferrite Nanoparticles: Role of Gd Doping Level", Nano-Structures & Nano-Objects. 2024, 40, 101327. Https://Doi.Org/10.1016/J.Nanoso.2024.101327 .
[5]. R. Sharma, S. Bansal, S. Singhal, Augmenting The Catalytic Activity Of Cofe2o4 By Substituting Rare Earth Cations Into The Spin Structure, RSC Adv. 2016, 6, 71676–71691. Https://Doi.Org/10.1039/C6RA14325C .
[6]. S. Rehman, M.A. Almessiere, N. Tashkandi, A. Baykal, Y. Slimani, R. Jermy, V. Ravinayagam, C. Yaman, Fabrication Of Spinel Cobalt Ferrite (Cofe2o4) Nanoparticles With Unique Earth Element Cerium And Neodymium For Anticandidal Activities, Chem. Sel. 2019, 4 14329–14334. Https://Doi.Org/10.1002/Slct.201901811 .
[7]. A.A. Sattar, A.M. Samy, R.S. El-Ezza, A.E. Eatah, Effect Of Rare Earth Substitution On Magnetic And Electrical Properties Of Mn–Zn Ferrites, Phys. Status Solidi 193 (2002) 86–93. Https://Doi.Org/10.1002/1521-396X(200209)193:1<86:AID-PSSA86>3.0.CO;2-i.
[8]. H. Nathani, S. Gubbala, R.D.K. Misra, Magnetic Behavior Of Nanocrystalline Nickel Ferrite: Part I. The Effect Of Surface Roughness, Mater. Sci. Eng. B 121 (2005) 126–136. Https://Doi.Org/10.1016/J.Mseb.2005.03.016 .
[9]. S.E. Jacobo, P.G. Bercoff, Structural And Electromagnetic Properties Of Yttrium-Substituted Ni–Zn Ferrites, Ceram. Int. 42 (2016) 7664–7668. Https://Doi.Org/10.1016/J.Ceramint.2016.01.180 .
[10]. R. Bortnic, A. Szatmari, T. Dragoiu, R.G. Hategan, R. Atanasov, L. Barbu-Tudoran, C. Tiusan, R. Lucacel-Ciceo, R. Dudric, R. Tetean, The Influence of Light Rare-Earth Substitution on Electronic and Magnetic Properties of Cofe(2)O(4) Nanoparticles., Nanometre. (Basel, Switzerland) 15 (2025). Https://Doi.Org/10.3390/Nano15151152 .
[11]. Hossain, M. D., Esha, I. N., Hossain, M. S., Ali, M. A., Khan, M. N. I., Hasan, M. R., Hakim, M. A., & Jamil, A. T. M. K. (2021). Impact of V Substitution on the Physical Properties of Ni–Zn–Co Ferrites: Structural, Magnetic, Dielectric and Electrical Properties. Materials Research Express, 8(4), 046102. Https://Doi.Org/10.1088/2053-1591/Abf6f7.
[12]. B.M. Bindushree, G. Chavan, L.R. Naik, R.F. Bhajantri, V. Gudihal, Effect of Yttrium Doping on the Physical Properties of Mg-Zn Ferrite: A Detailed Study, Next Mater. 9 (2025) 101247. Https://Doi.Org/10.1016/J.Nxmate.2025.101247.
[13]. G.M. Shweta, L.R. Naik, R.B. Pujar, S.N. Mathad, Influence of Magnesium Doping on Structural and Elastic Parameters of Nickel Zinc Nanoferrites, Mater. Chem. Phys. 257 (2021) 123825. Https://Doi.Org/10.1016/J.Matchemphys.2020.123825.
[14]. S.K. Ray, J. Cho, J. Hur, A Critical Review on Strategies for Improving Efficiency of Batio3-Based Photocatalysts for Wastewater Treatment, J. Environ. Manage. 290 (2021) 112679. Https://Doi.Org/10.1016/J.Jenvman.2021.112679 .
[15]. A.S. Waingankar, S.G. Kulkarni, M.S. Sagare, J. Phys. IV, 1997, 155.
[16]. R.S. Devan, Y.D. Kolekar, B.K. Chougule, J. Phys.: Condens. Matter, 2006, Doi :10.1088/0953-8984/18/43/004
[17]. H. Bozetine, S. Meziane, S. Aziri, N. Berkane, D. Allam, S. Boudinar, T. Hadjersi, Bulletin of Materials Science, 2021, 44, 64. Doi: 10.15251/DJNB.2021.164.1209.
[18]. S. Sindhu, M.R. Anantharaman, B.P. Thampi, K.A. Malini, P. Kurian, Evaluation of A.C. Conductivity of Rubber Ferrite Composites from Dielectric Measurements, Bull. Mater. Sci. 25 (2002) 599–607. Https://Doi.Org/10.1007/BF02707892.
[19]. M.K. Anupama, B. Rudraswamy, N. Dhananjaya, Investigation on Impedance Response and Dielectric Relaxation of Ni-Zn Ferrites Prepared by Self-Combustion Technique, J. Alloys Compd. 706 (2017) 554–561. Https://Doi.Org/10.1016/J.Jallcom.2017.02.241 .
[20]. H. El Moussaoui, T. Mahfoud, S. Habouti, K. El Maalam, M. Ben Ali, M. Hamedoun, O. Mounkachi, R. Masrour, E.K. Hlil, A. Ben Youssef, Synthesis and Magnetic Properties of Tin Spinel Ferrites Doped Manganese, J. Magn. Magn. Mater. 405 (2016) 181–186. Https://Doi.Org/10.1016/J.Jmmm.2015.12.059 .
[21]. X. Niu, B. Zong, H. Hu, B. Wu, Influence of Sn4+-Substituted on the Magnetic Properties and Power Loss of Ni-Zn Soft Magnetic Ferrites, Optik (Stuttg). 134 (2017) 135–139. Https://Doi.Org/10.1016/J.Ijleo.2017.01.043 .
[22]. S.N. Patil, A.M. Pawar, S.K. Tilekar, B.P. Ladgaonkar, Investigation of Magnesium Substituted Nano Particle Zinc Ferrites for Relative Humidity Sensors, Sensors Actuators A Phys. 244 (2016) 35–43. Https://Doi.Org/10.1016/J.Sna.2016.04.019 .
[23]. S.S. Bellad, S.C. Watwe, B.K. Chougule, Mater. Res. Bull. 1999, 37, 7, 1099. Https://Doi.Org/10.1063/1.3606319.
[24]. Sarita, Anchal, Priya, R.K. Beniwal, M.S. Rulaniya, P.M. Saini, P. Yadav, U. Kumar, Aakansha, P.A. Alvi, B.L. Choudhary, Development and Characterization of Superparamagnetic Zn-Doped Nickel Ferrite Nanoparticles, J. Magn. Magn. Mater. 610 (2024) 172547. Https://Doi.Org/10.1016/J.Jmmm.2024.172547.
[25]. L. Xiaolong, D. Yaqiang, L. Min, C. Chuntao, W. Xin-Min, New Fe-Based Amorphous Soft Magnetic Composites with Significant Enhancement of Magnetic Properties by Compositing with Nano-(Nizn) Fe2O4, J. Alloys Compd. 696 (2017) 1323–1328. Https://Doi.Org/10.1016/J.Jallcom.2016.11.241.

[26]. S. Hasan, B. Azhdar, Cation Distribution and Microstructure Effects on Structural, Elastic, And Dielectric Properties Of (Co, Ni)0.5Cd0.5Fe2O4 Nanoparticles, Appl. Phys. A 131 (2025) 1025.Https://Doi.Org/10.1007/S00339-025-09155-W .

[27]. P. Samoila, C. Cojocaru, L. Sacarescu, P.P. Dorneanu, A.-A. Domokos, A. Rotaru, Remarkable Catalytic Properties of Rare-Earth Doped Nickel Ferrites Synthesized by Sol-Gel Auto-Combustion with Maleic Acid as Fuel for CWPO Of Dyes, Appl. Catal. B Environ. 202 (2017) 21–32. Https://Doi.Org/10.1016/J.Apcatb.2016.09.012 .

[28]. N.A. Algarou, Y. Slimani, M. A. Almessiere, A. Baykal, Exchange-Coupling Behavior in Srtb0.01Tm0.01Fe11.98O19/(Cofe2o4) X Hard/Soft Nanocomposites, New J. Chem. 44 (2020) 5800–5808. Https://Doi.Org/10.1039/D0NJ00109K .

[29]. V. V Atuchin, D.A. Vinnik, T.A. Gavrilova, S.A. Gudkova, L.I. Isaenko, X. Jiang, L.D. Pokrovsky, I.P. Prosvirin, L.S. Mashkovtseva, Z. Lin, Flux Crystal Growth and the Electronic Structure of Bafe12o19 Hexaferrite, J. Phys. Chem. C 120 (2016) 5114–5123. Https://Doi.Org/10.1021/Acs.Jpcc.5b12243.

[30]. D.A. Vinnik, D.S. Klygach, V.E. Zhivulin, A.I. Malkin, M.G. Vakhitov, S.A. Gudkova, D.M. Galimov, D.A. Zherebtsov, E.A. Trofimov, N.S. Knyazev, V. V Atuchin, S. V Trukhanov, A. V Trukhanov, Electromagnetic Properties of Bafe12019: Ti at Centimetre Wavelengths, J. Alloys Compd. 755 (2018) 177–183. Https://Doi.Org/10.1016/J.Jallcom.2018.04.315 .

[31]. M.K. Rendale, S.N. Mathad, Resonance Shifting by Ferrite Thick Film Superstrate, Serbian J. Electr. Eng. 2018, 15, 3, 275–284. Https://Doi.Org/10.2298/SJEE1803275R.

[32]. R. Sharma, P. Thakur, P. Sharma, V. Sharma, "Ferrimagnetic Ni2+Doped Mg-Zn Spinel Ferrite Nanoparticles for High Density Information Storage", J. Alloys Compd. 2017, 704, 7–17. 10.1016/J.Jallcom.2017.02.021 .

[33]. Kim, Y.I., Kim, D. And Lee, C.S. (2003) Synthesis and Characterization of Cofe2o4 Magnetic Nanoparticles Prepared by Temperature-Controlled Coprecipitation Method. Physica B: Condensed Matter, 337, 42-51. Https://Doi.Org/10.1016/S0921-4526(03)00322-3 .

[34]. C. Caizer, M. Popovici, C. Savii, Spherical (Znδni1-Δfe2o4) Γ Nanoparticles in an Amorphous (Sio2)1-Γ Matrix, Prepared with the Sol–Gel Method, Acta Mater. 51 (2003) 3607–3616. Https://Doi.Org/10.1016/S1359-6454(03)00178-2 .

[35]. J.A. López Pérez, M.A. López Quintela, J. Mira, J. Rivas, S.W. Charles, Advances in the Preparation of Magnetic Nanoparticles by The Microemulsion Method, J. Phys. Chem. B 101 (1997) 8045–8047. Https://Doi.Org/10.1021/Jp972046t .

[36]. Q. Chen, Z.J. Zhang, "Size-Dependent Superparamagnetic Properties of Mgfe2o4 Spinel Ferrite Nano crystallites", Appl. Phys. Lett. 1998, 73, 3156–3158. Https://Doi.Org/10.1063/1.122704 .

[37]. C.T. Seip, E.E. Carpenter, C.J.O. Connor, V.T. John, Sichu Li, "Magnetic Properties of a Series of Ferrite Nanoparticles Synthesized in Reverse Micelles", IEEE T MAGN. 1998, 34, 1111–1113.

[38]. J.F. Hochepied, P. Bonville, M.P. Pileni, Nonstoichiometric Zinc Ferrite Nanocrystals: Syntheses and Unusual Magnetic Properties, J. Phys. Chem. B 104 (2000) 905–912. Https://Doi.Org/10.1021/Jp991626i .

[39]. H. Hussein, S.S. Ibrahim, S.A. Khairy, Biosynthesis of Cofe2o4 Ferrite Nanoparticles Using Greek Yogurt Solution: Deep Structural Insights and Appraisal for Ecological Mitigation Via Quartz Crystal Microbalance, J. Water Process Eng. 65 (2024) 105856. Https://Doi.Org/Https://Doi.Org/10.1016/J.Jwpe.2024.105856 .

[40]. A. Cottrell, An Introduction to Metallurgy, Edward Arnold Publishing Ltd., London, 1967.

[41]. B. Süngü Mısırlıoğlu, N.D. Kahya, Z. Öztürk, Enhanced Dielectric Properties of Copper Substituted Nickel Ferrite Nanoparticles for Energy Storage Applications, J. Phys. Chem. Solids 193 (2024) 112195. Https://Doi.Org/10.1016/J.Jpcs.2024.112195.

[42]. Modi, K. B. (2004). Elastic Moduli Determination Through IR Spectroscopy for Zinc Substituted Copper Ferri Chromates. Journal Of Materials Science, 39(8), 2887–2890. Https://Doi.Org/10.1023/B:Jmsc.0000021472.00590.9b .

[43]. G. Bonsdorf, M.A. Denecke, K. Schäfer, S. Christen, H. Langbein, W. Gunßer, X-Ray Absorption Spectroscopic and Mössbauer Studies of Redox and Cation-Ordering Processes in Manganese Ferrite, Solid State Ionics 101–103 (1997) 351–357. Https://Doi.Org/Https://Doi.Org/10.1016/S0167-2738(97)84052-0 .

[44]. G. Bonsdorf, M.A. Denecke, K. Schäfer, S. Christen, H. Langbein, W. Gunßer, X-Ray Absorption Spectroscopic and Mössbauer Studies of Redox and Cation-Ordering Processes in Manganese Ferrite, Solid State Ionics 101–103 (1997) 351–357. Https://Doi.Org/10.1016/S0167-2738(97)84052-0.

[45]. P.C. Patil, A.A. Gaikwad, V.P. Phase, R.H. Kadam, S.E. Shirsath, J.J. Chamargore, Rare Earth Ce and Y Cation Co-Substitution and Its Effects on the Strain, Elasticity, And Magnetism of Co-Zn Ferrite Nanomaterials, Ceram. Int. 51 (2025) 21675–21688. Https://Doi.Org/10.1016/J.Ceramint.2025.02.329 .

[46]. M.A. Ali, M.N.I. Khan, F.-U.-Z. Chowdhury, M.M. Hossain, M.Z. Rahaman, S.M. Hoque, M.A. Matin, M.M. Uddin, Study of Physical Properties Towards Optimizing Sintering Temperature Of Y-Substituted Mg-Zn Ferrites, Results Phys. 14 (2019) 102517. Https://Doi.Org/10.1016/J.Rinp.2019.102517.

[47]. R. Tholkappiyan, K. Vishista, NN-Methylene Bis Acrylamide: A Novel Fuel for Combustion Synthesis of Zinc Ferrite Nanoparticles and Studied by X-Ray Photoelectron Spectroscopy, Int J. Chemtech. Res. 2014, 6 2834–2842.

[48]. S. Joshi, M. Kumar, S. Chhoker, G. Srivastava, M. Jewariya, V.N. Singh, Structural, Magnetic, Dielectric and Optical Properties of Nickel Ferrite Nanoparticles Synthesized by Co-Precipitation Method, J. Mol. Struct. 1076 (2014) 55–62. Https://Doi.Org/10.1016/J.Molstruc.2014.07.048 .

[49]. N.S. Al-Bassami, S.F. Mansour, M.B.M. Yusuf, N. Usha, N.H. Alsmail, M.A. Abdo, Yttrium-Induced Modification of Structural, Magnetic, Optical, And Photocatalytic Characteristics in Ni-Zn–Mn Nano ferrites for Versatile Applications, Ceram. Int. 52 (2026) 7436–7449. Https://Doi.Org/10.1016/J.Ceramint.2025.12.484 .

[50]. P.B. Belavi, G.N. Chavan, L.R. Naik, R. Somashekar, R.K. Kotnala, Structural, Electrical and Magnetic Properties of Cadmium Substituted Nickel–Copper Ferrites, Mater. Chem. Phys. 132 (2012) 138–144. Https://Doi.Org/10.1016/J.Matchemphys.2011.11.009

[51]. P. Chavan and L.R. Naik, Int. J. Eng. Sci. Res. 2016, 6, 29. Doi: 10.1007/S11664-016-4886-6.

[52]. A.B. Mugutkar, S.K. Gore, R.S. Mane, S.M. Patange, S.S. Jadhav, S.F. Shaikh, A.M. Al-Enizi, A. Nafady, B.M. Thamer, M. Ubaidullah, Structural Modifications In Co–Zn Nano ferrites by Gd Substitution Triggering to Dielectric and Gas Sensing Applications, J. Alloys Compd. 844 (2020) 156178. Https://Doi.Org/10.1016/J.Jallcom.2020.156178 .

[53]. K. Iwauchi, Jpn. J. Appl. Phys. 10, 1520 (1971). Doi :10.1143/JJAP.10.1520.

[54]. G. Lal, K. Punia, H. Bhoi, S.N. Dolia, B.L. Choudhary, P.A. Alvi, S. Dalela, S.K. Barbar, S. Kumar, Exploring the Structural, Elastic, Optical, Dielectric and Magnetic Characteristics of Ca2+ Incorporated Superparamagnetic Zn0.5−Xca0.1Co0.4+Xfe2o4 (X = 0.0, 0.05 & 0.1) Nano ferrites, J. Alloys Compd. 886 (2021) 161190. Https://Doi.Org/10.1016/J.Jallcom.2021.161190 .

[55]. Jogi, J. K., Singhal, S. K., Jangir, R., Tanna, A., Singh, A., Hirpara, B., & Shah, N. (2024). Laser Irradiation Effects on the Dielectric Properties of Zinc Ferrite at Room Temperature. Radiation Effects and Defects in Solids, 179(3–4), 358–370. Https://Doi.Org/10.1080/10420150.2023.2278139 .

[56]. M.A. Bhatt, A.R. Tanna, Effect of Li-Ion Doping on Structural, Optical and Electrochemical Properties of V2O5, J. Mater. Sci. Mater. Electron. 34 (2023) 2146. Https://Doi.Org/10.1007/S10854-023-11462-Y .

[57]. H.H. Qiu, T. Ito, H. Sakata, DC Conductivity of Fe2O3–Bi2O3–B2O3 Glasses, Mater. Chem. Phys. 58 (1999) 243–248.

Https://Doi.Org/10.1016/S0254-0584(98)00281-8 .
[58]. D. Chavan, D.P. Belavi, Studies on Electrical and Magnetic Properties of Mg-Substituted Nickel Ferrites, J. Electron. Mater. (2016). Https://Doi.Org/10.1007/S11664-016-4886-6.
[59]. S.E. Jacobo, P.G. Bercoff, Structural and Electromagnetic Properties of Yttrium-Substituted Ni–Zn Ferrites, Ceram. Int. 42 (2016) 7664–7668. Https://Doi.Org/10.1016/J.Ceramint.2016.01.180 .
[60]. S. S. Satpute1, S. R. Wadgane2, K. Desai3, D. R. Mane4, R. H. Kadam, "Substitution Effect of Y3+ Ions on the Structural, Magnetic and Electrical Properties of Cobalt Ferrite Nanoparticles", Ceramic. 2020, 66, 43-49. Https://Doi.Org/10.1590/0366-69132020663772734 .
[61]. N. Khatun, S. Ahmed, M.S. Hossain, S.F. Uddin Farhad, M. Al Mamun, M.S. Alam, M.H.A. Begum, N.I. Tanvir, M. Hakim, S. Islam, Influence of Y3+ And La3+ Ions on the Structural, Magnetic, Electrical, And Optical Properties of Cobalt Ferrite Nanoparticles, Heliyon 9 (2023) E13019. Https://Doi.Org/10.1016/J.Heliyon.2023.E13019 .